Electrochemical and Tribological Behavior of Oxide Dispersion Strengthened Duplex Stainless Steel in Mine Water Environment

O. Olaniran[1,2*]

[1] *Department of Metallurgical and Materials Engineering, Federal University of Technology, Akure*
[2] *Department of Chemical Engineering, University of Johannesburg, Johannesburg, South Africa*

ARTICLE INFO

ABSTRACT

This work investigates the electrochemical and aqueous tribological behavior of hot pressed 2205 duplex stainless steel (DSS). DSS sintered composites of different volume percentages (% vol) of partially stabilized zirconia (PSZ) were developed using powder metallurgy (PM) technique. Electrochemical behavior was studied at room temperature, using open circuit potential and potentiodynamic scanning in simulated mine water and 3.5% NaCl solution, while aqueous tribological test was carried out in simulated mine water. The influence of PSZ, Cr and Ni additions on the degradation mechanisms of corrosion and wear of the modified DSS was evaluated. X-Ray Microtomography (XRM) was used as experimental technique for defect analysis from the corrosion studies. The obtained results show the surface imaging capability of SEM and the internal structures imaging capability of XRM. SEM revealed important surface degradation mechanisms of the materials, while relevant information on the pitting corrosion was obtained from XRM. It was concluded that the pitting corrosion can be caused by the growth of intergranular corrosion resulting from the attack and the breakdown of passive films by chloride ions which affected both the surface and the internal parts of the samples.

1-Introduction

Service requirements in many industries such as oil and gas, chemical and mining necessitate the development of improved stainless steels with superior properties. Combination of dissimilar materials for new applications creates interfaces whose properties and processing need to be understood before they can be applied commercially [1]. Improving the overall properties of stainless steels in turn requires the selection of effective materials and development techniques. Available synergistic approaches include the manipulations and modifications of the metallurgical influencing parameters through phase modification and transformation, microstructural modification, and control of alloy composition [2]. In addition to the above approaches, the overall improvement of stainless steel properties can be achieved through the selection of effective production process. The powder metallurgical method offers an efficient technique for the fabrication of metal– ceramic composites and provides a uniform distribution of particulates in the composites [3, 4]. Among the various means which the overall properties of powder metallurgy stainless steel components can be improved, two major approached are very

* Corresponding author:
  E-mail: oladayolaniran@gmail.com

critical. The first is the reinforcement with selected additives while the second is the improvement of sintering techniques. According to [3], there is a considerable scope for improving the properties of powder metallurgy components through novel sintering techniques and/or by alloying additives. However, corrosion resistance of sintered stainless steel is lower than that of either cast or wrought stainless steels, inherent residual open porosity being mainly responsible for this behavior [5].

Among various processing techniques for improving the corrosion resistance of ferrous metals, a useful approach involves coating and alloying. There is a continuous need for coated metallic components for wear and corrosion protection. These coatings are expected to exhibit both a high wear and corrosion resistance with a good adhesive bonding to the metallic component [6, 7]. As an alternative to the pure ceramic coatings, many methods have been utilized to develop metal-ceramic composites. It was however found that no sufficient adhesive bonding was achieved [6]. However, this poses considerable difficulties from the manufacturing point of view. This serves powder metallurgy an excellent alternative to produce stainless steel [8]. Also, the use of oxide dispersion strengthening to improve the mechanical properties of stainless steels has been reported with good results [9, 10, 11]. However, the usage in automobile parts is still weak in many parts of the world, which is the reason for advanced research on the sintered stainless steel composite especially for its ease of manufacturing, cost effectiveness and environmentally friendliness [12]. Current studies therefore focus on the influence of PSZ, Cr and Ni on the electrochemical and aqueous tribological behavior of DSS composite produced by PM technique in and mine water.

2-Materials and Methods

A mixture of atomized polychrystalline 2205 duplex stainless steel whose chemical composition is presented in Table 1, partially stabilized Zirconia (PSZ, 3% yttria, mole fraction), Chromium and Nickel was used in this study. The powders particle sizes as stated

by the suppliers are: Duplex stainless steel (2205)= 22 μm, partially stabilized Zirconia (PZY)= 50 nm, Chromium and Nickel= 325 mesh and 4.5 μm, respectively. XRD was used to determine the phases. Different composites were produced by weighing different percentages of the matrix, the reinforcement and the alloying elements as indicated in Table 2. These weighed powders were mixed in the TUBULAR® mixer for 2 hours.

The mixed powders were sintered in a hot press at 1100°C, under 30 MPa pressure and 30 minutes holding time using argon gas flow to achieve a consolidated bulk cylindrical composite of 18 mm diameter and 2 mm thickness. Scanning electron microscope (SEM) equipped with energy dispersive X-ray spectroscopy (EDS) (model JEOL, JSM – 7600FA) was used to assess the shape, agglomeration of particles and the compositions of the various ODS composites. Phase identification was carried out using X-ray diffraction PANanalytical X'pert PRO with the Co anode, and a step size of 2θ (generating settings 30 kV, 10 mA). The densities of the sintered samples were measured using the Archimedes principle after separately weighing in air and water using an electronic balance of 0.1 mg precision. Morphology, shape, and size distribution of the phases in the sintered components were studied using field emission scanning electron microscopy (FESEM). Relative density was calculated from the sintered density and theoretical density, the latter was deduced from the simple law of mixture; $\rho t = \rho 1 f 1 + \rho 2 f 2 + ... + \rho n f n$, where ρi and $f i$ are the theoretical density and the volume fraction of component i.

The specimens for electrochemical testing were prepared by grinding to 1200 surface finish with SiC grit papers and polished to 3 μm using diamond suspension. The specimens were ultrasonically cleaned in ethanol before immersion in electrolyte for corrosion testing. Open circuit potentials and potentiodynamic polarization were used to obtain information about the corrosion behavior of the sintered samples in simulated mine environment (Table

3). The corrosion experiments were carried out using an Autolab Potentiostat with general purpose electrochemical system software (GPES 4.9). All the experiments were carried out using a three-electrode corrosion cell setup with saturated Ag/AgCl as reference and graphite rod as counter electrode. All the tests were conducted at room temperature (20±2 °C) and repeated twice while the average was recorded. Polarization measurements were carried out using a scan rate of 2 mVs^{-1} at a potential initiated at −1000 mV to +1500 mV from corrosion potential.

The sliding wear test was conducted using a ball-on-disc tribometer (UM-2, center for Tribology Inc. Brooker Nano Inc (CETR),

Cambell, CA), to assess the wear behavior of specimens in reciprocating wet sliding condition. The specimens for wear testing were cut into sizes of 2 × 2 × 0.3 cm and wet ground using a series of SiC grinding papers down to the 3 μm, followed by cleaning with running water and ethanol. Tungsten carbide (WC) ball with diameter of 10 mm was used as the counter surface. The wear tests were carried out at an applied load of 25 N under ambient temperature at a frequency of 5 Hz. The stroke length was 2 mm. The coefficient of friction (COF) was continuously monitored during sliding condition. The experiment was also repeated twice while the average was recorded.

Table 1. Elemental composition of the as-received 2205 powders (wt%).

Cr	Ni	Mo	Si	N	P	C	Mn	S	Fe
22.8	5.1	3.3	0.77	0.25	0.014	0.012	0.98	0.006	Bal

Table 2. Powder composition of 2205 duplex stainless steel composites (wt%).

Sample no	2507 Composition %	ZrO$_2$(Y$_2$O$_3$) %	Cr %	Ni %
X	100	-	-	-
A1	99.50	0.50	-	-
A2	98.50	0.50	0.815	0.185
A3	97.0	1	1.63	0.37
A4	95.0	2	1.63	0.37
A5	95.0	3	2.44	0.36

Table 3. Composition of simulated mine water.

S/N	Compound	Quantity
1	Distilled water	1 L
2	Sodium Sulphate	1.237g
3	Magnesium Sulphate	1.99g
4	Calcium Chloride	1.038
5	Sodium Chloride	1.380g

3-Results and Discussion

Figure 1 shows the variation of open circuit potential (OCP) of the ODS DSS composites. The curves displayed a similar behavior for all the samples. There was a n initial shift in the more negative potential i.e. the active region for the first few seconds, after which

there was a slight shift back to the more positive region, an indication of passivation. The potential was then stabilized, which was maintained for almost all the duration of the experiment. However, sample A1 showed the most negative potential followed by sample X (sintered as-received), while sample A2 had

the most positive potential. The indication of this was that sample A1 has the most corrosion susceptibility followed by the as-received 2205 (X). Other samples, i. e. A2, A3 and A4 are less corrosion susceptible than sintered as-received 2205 in simulated mine water. This could be linked to high percentage of chromium [12, 13, 14]. Sample A5, on the other hand, at the initial stage of the experiment showed a higher potential, but over time it shifted to a lower potential compared with sample X.
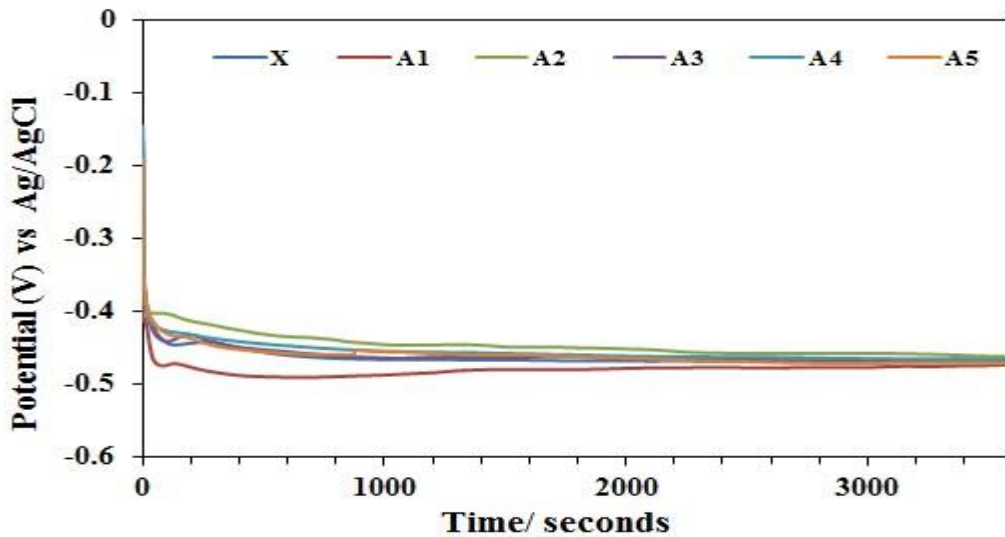

Fig. 1. OCP measurement for 2205 DSS composites in simulated mine water.

Addition of PSZ with Chromium and Nickel to 2205 DSS influences the polarization potential by shifting the potentials into the more positive region as can be observed in samples A1, A2 and A5 in Figure 1. However, for samples A3 and A4, the potentials were shifted to the active region which indicated that corrosion susceptibility of samples A3 and A4 are higher than that of samples A1, A2 and A5. From the graphs, it was seen that sample A5 has the highest potential with the most shift in the positive potential.
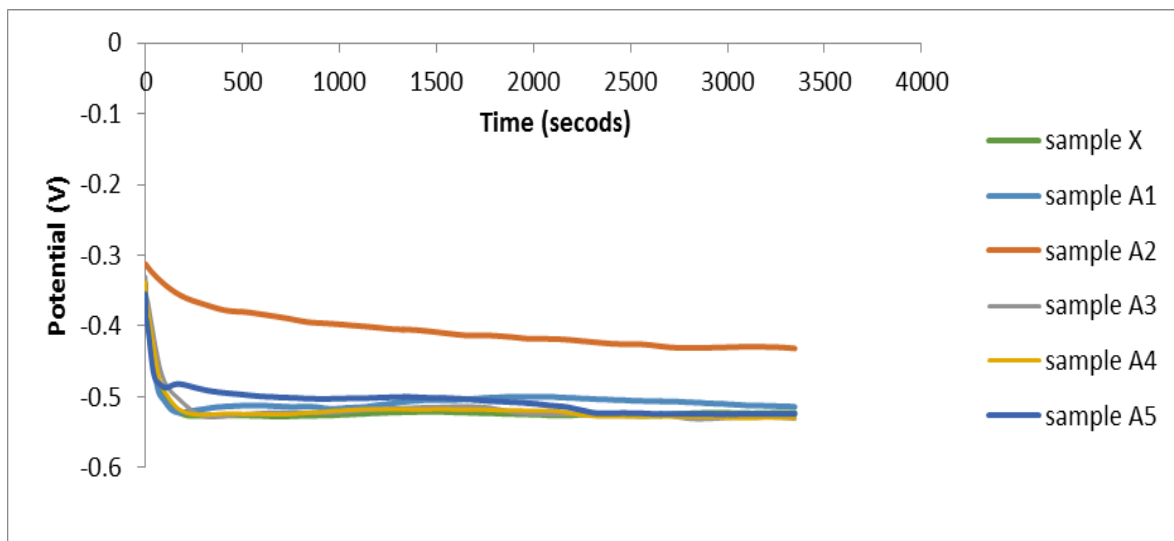

Fig. 2. OCP measurement for 2205 DSS composites in 3.5% NaCl.

On the other hand, Figure 2 shows the OCP for 2205 ODS DSS in 3.5% NaCl. It was observed that sample Y has the most positive potential which indicated that the addition of PSZ has shifted the potential to the more negative region, showing that they are more prone to corrosion attack in 3.5% NaCl solution.

Potentio-dynamic polarization experiment was carried out to study the electrochemical behavior of the sintered DSS composites in both simulated mine water and 3.5% NaCl solution. The polarization curves were obtained under the same conditions after 25 minutes of the composite immersion in simulated mine water at room temperature. The Values of corrosion potentials, corrosion current densities and corrosion rates were calculated from polarization curves for the various samples.
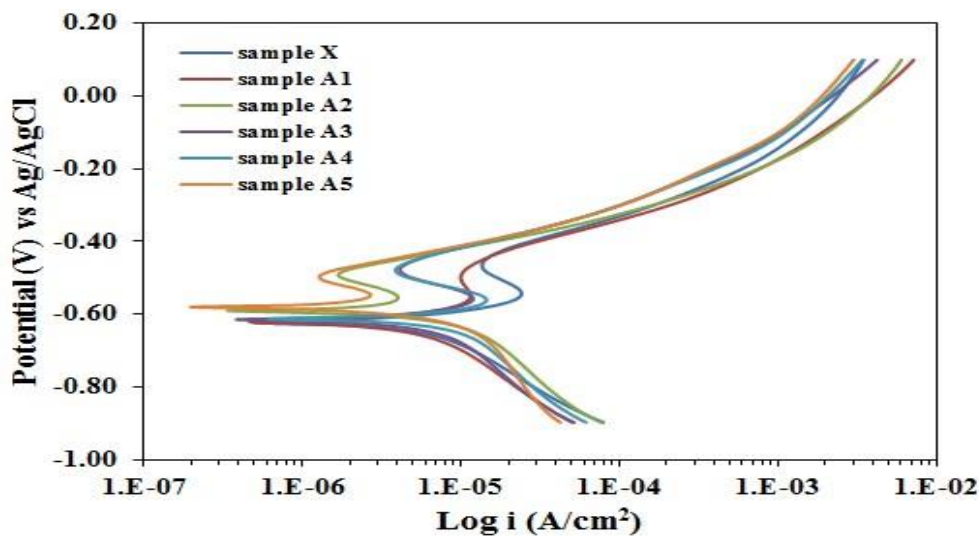

Fig. 3. Polarization curves of PM 2205 DSS composite in simulated mine water.

Figure 3 shows the potentio-dynamic polarization curves for each composite of 2205 and its composites. Taking composite X as the referential point, the potential of composite A1 was shifted to the more negative potential while A3 and A4 were slightly shifted to the more negative potential but A2 was almost the same as composite X. It could be possibly due to the fact that the incorporation of the dispersant (PSZ) has destabilized the balance of the original composition of the 2205 DSS in A1 and there was no further addition of Cr to positively affect the corrosion properties as shown in the corrosion current density. However, for composite samples A2, A3 and A4, though there were further incorporation of Cr and Ni, the Cr present might not be enough to maintain the balance in the chemical composition or inhomogeneity in the composite or even combination of both. For composite A5, the potential was shifted in the more positive potential. The implications of this was that A5 with the most positive potential has the least susceptibility to corrosion while sample A1 with the least potential has the highest susceptibility to corrosion. Similar trend was observed from the corrosion current density which indicated that composite A5 has the least corrosion rate; A5 has the least corrosion rate as shown in Table 3. This could be connected to the percentage of Cr and Ni present in the composite matrix (2.4% Cr and 0.56% Ni). This clearly demonstrated that the Cr present in this composite is well enough to convert all the available carbon to carbide thereby suppressing the corrosion reaction rate as indicated from the current density. However, in sample A4, the Cr present is enough also to convert the carbon to carbide but the corrosion reaction might have been influenced by inhomogeneity due to high percentage of PSZ (3%) [2]. Also from the curves, there were region of passivation.

Table 3. Corrosion rate of 2205 DSS composites in simulated mine water.

Sample	Ecorr (mV)	icorr(A)	Icorr(A/cm^2)	bc(v/dec)	ba(v/dec)	Rp(Ω)	Cr(mm/yr)
X	-0.628	5.82E^{-6}	4.096E^{-6}	0.116	0.229	1.972E^3	4.844E^{-2}
A1	-0.625	2.57E^{-6}	2.545E^{-6}	0.082	0.101	1.397E^3	3.024E^{-2}
A2	-0.595	1.70E^{-6}	1.487E^{-6}	0.086	0.035	7.573E^2	1.769E^{-2}
A3	-0.617	3.55E^{-6}	2.793E^{-6}	0.088	0.124	1.335E^3	3.307E^{-2}
A4	-0.619	6.05E^{-6}	4.767E^{-6}	0.138	0.161	1.586E^3	5.657E^{-2}
A5	-0.583	7.13E^{-7}	5.612E^{-7}	0.04	0.023	5.536E^2	6.68E^{-3}

On the other hand, nickel shows more grain refinement; this is another important factor that helps in heat resistance of steel (oxidation prevention). As a consequence, nickel helps to increase the toughness of steel at low temperature when present in moderate [15].

The SEM image revealed that the addition of PSZ and Cr with Ni enhanced the corrosion property. However, the SEM image was characterized by development and growing of pits. These pits were found to be clustering around a region but they were found not to develop around the PSZ.
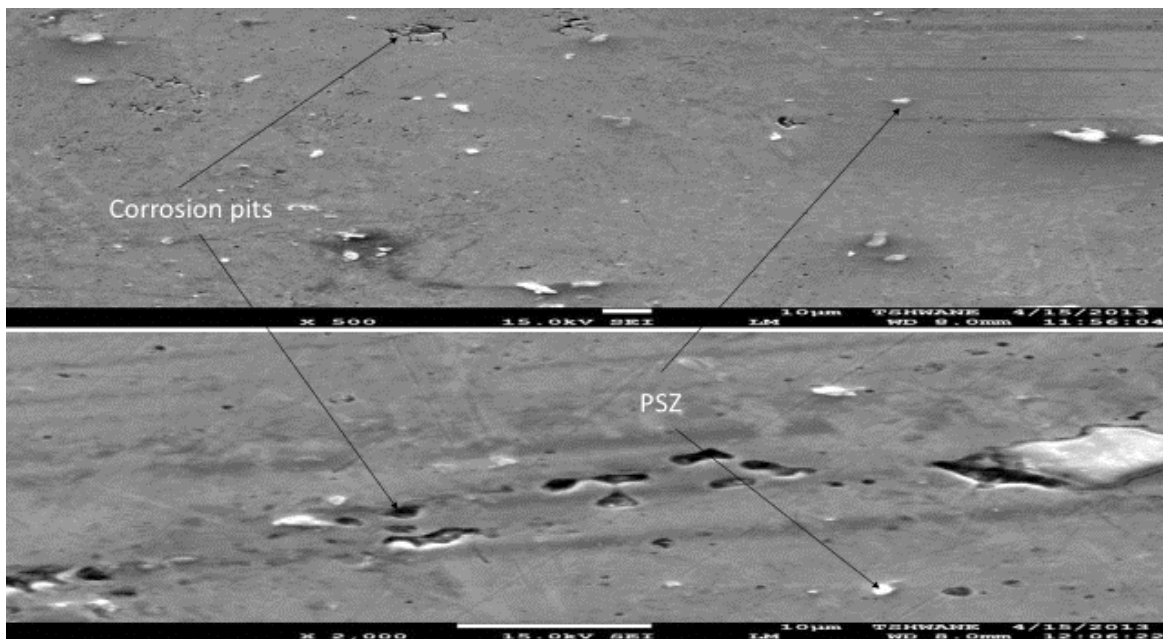

Fig. 4. Typical SEM image of the corroded sample in simulated mine water at different magnifications.
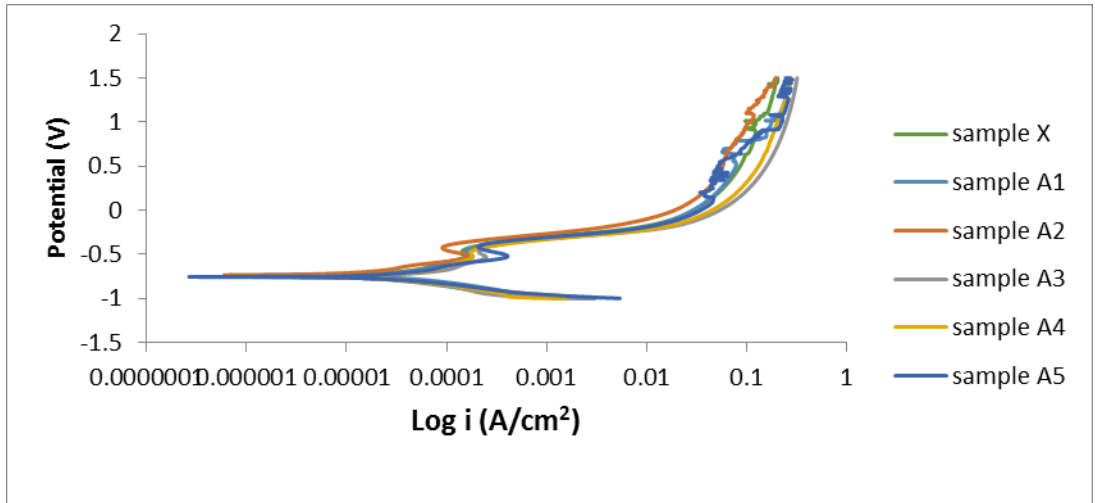
Fig. 5. Polarization curve of 2205 DSS composite in 3.5% NaCl.

Potentiodynamic polarization curves for 2205 ODS DSS in 3.5% NaCl solution are represented in Figure 5. It was observed that sample A2 has the highest corrosion potential although slightly higher than the rest of the samples, while sample A5 has the least potential but the highest corrosion current density which could mean inhomogeneity in the mixture. In a certain region, all the samples displayed passivation after which the reaction continues possibly due to the breakage of the passive film by chloride ions.
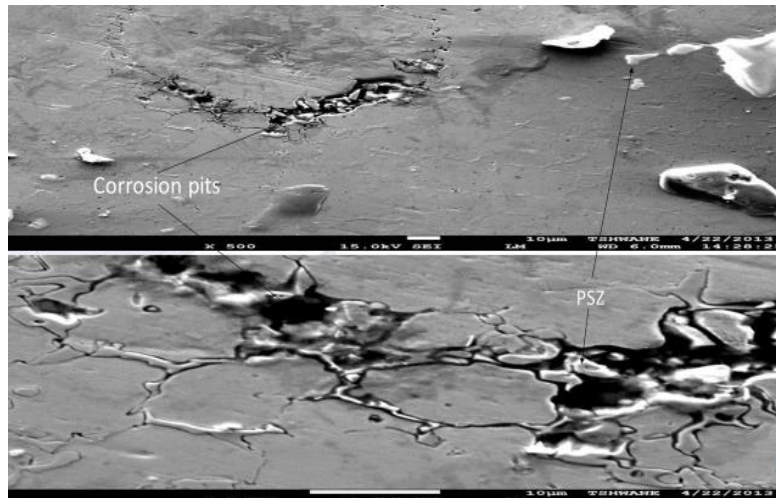

Fig. 6. Typical SEM image of the corroded sample in NaCl at different magnifications.

The SEM image (Figure 6) showed that the observed pits were formed as a result of chloride ion attack and were found to populate in a local region on the surface of the composites forming circular clusters. The types of pits formed were similar to corrosion pits formed on wrought 2209 duplex stainless steel reported by [16]. This phenomenon could indicate that the attacks on the steel at pitting sites were possibly initiated as a result of certain inhomogeneity in the steel and concentration gradient of the chloride ions. However, it was also observed that the pits did not originate around the ODS but on the weaker section of the stainless steel which demonstrated that oxide dispersion strengthening is not detrimental to corrosion property of the composite rather, and the PSZ

acts as barrier to the growth of pits within the composite.

3-1-Analysis of corrosion pits by XRM

Corrosion attack by chloride may develop within the pores beneath the surface, excess porosity may expose the core material to corrosive environment by increasing the surface area. In this case, the superior surface appearance of a sintered part may be misleading and as the demand for quality control on components used in many engineering sectors is very stringent and critical to their safe and efficient usage, materials reliability must be ascertained. SEM evaluation of the corrosion pits involving sample cross sectioning to view and measure the depth of attack are however often imprecise, destructive and time consuming. While conventional imaging tools as optical microscopy and AFM are adequate to visualize surface structures, it has been difficult to accurately characterize their internal 3D arrays and functionalities [17]. In order to effectively understand the nature of defects and/or damages on materials, it is imperative to non-destructively characterize such defects/damages in 3D mode using x-ray microtomography technique.

Images of high resolution scans were obtained on relative smaller sizes of the corroded sample at longer times, Voxel size of 0.93 μm, and field of view of 0.93 mm are shown in Figures 7a and b. The scanning was carried out to obtain more buried structural and morphological details about the typical region of corrosion at different depths (Figure 7a), while reconstruction is represented in Figure 7b to show the depth of damages.

Figure 7a is the typical images of the samples at the corroded surface, corrosion region just below the surface of the steel, and deep inside the steel where there was no corrosion attack. From Figure 7b, it was observed that corrosion pits on the surfaces of the steel showed evidences of penetration towards the inside of the steel. Typical XY slice of the corroded sample further revealed that the inside of the sample immersed in solution showed corrosion structure of uniform corrosion attack. It was further observed that the structure of the pit formed had a kidney shape buried within the steel. This indicated that the attack was initiated at the surface, grew down and expanded inside the steel composite. Virtual slice of the corrosion attack region below the surface revealed the buried pits of varying morphologies, geometries, and dimensions.
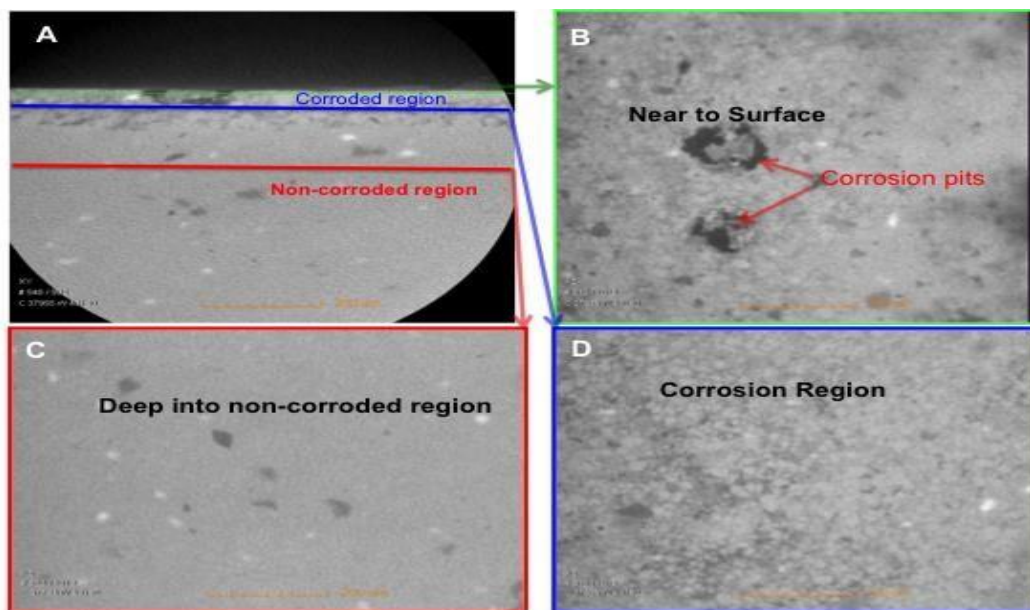

Fig. 7a. Typical high-resolution XRM images of the samples at different regions of corrosion attack.
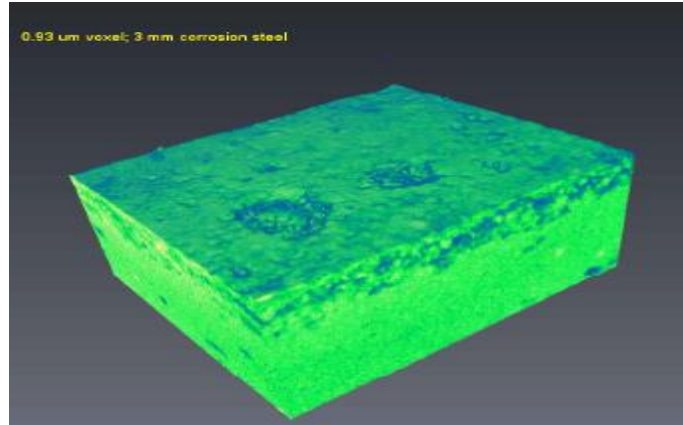
Fig. 7b. Three-dimensional rendering image from high resolution scanning showing the structure of corrosion damages within the steel.

3-2- Tribological Investigations

Wet wear was performed on the composite. The test was done under a load of 25 N with the oscillating frequency of 5Hz at room temperature.

The coefficient of friction increased fairly with increasing ceramic oxide and Ni-Cr content. As the inclusions in the samples increased, the graph showed that the COF increases with the increase in reinforcements. Sliding condition made materials undergo plastic deformation which finally results in surface rupture with a rapid rise in wear and friction.
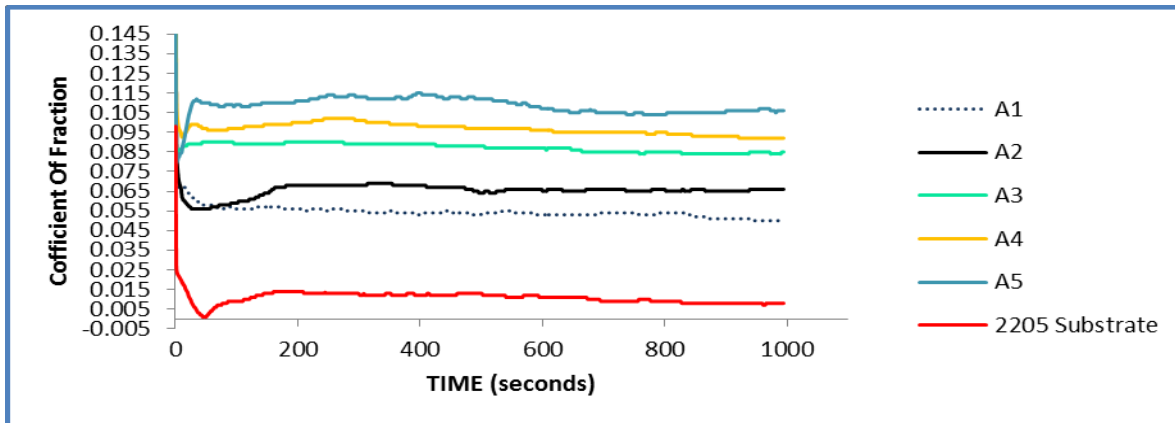

Fig. 8. Wet wear COF of DSS 2205 composites under the wear load of 25N and oscillating frequency of 5Hz.

Figure 8 shows the coefficient of friction with time for the composites in simulated mine water under the wear load of 25N. The results indicated that sintered as-received 2205 had the least COF while A5 retained its least wear property. This shows that at a certain condition, increase in the percentage of PSZ also increases the COF of the composites. It was expected that the COF should be reduced because of the hardness with increasing the PSZ content; however, this increase in the COF could possibly be linked to two different factors; (i) the high load which could activate the third body wear mechanism [15] and, (ii) corrosion attack on the substrate. Or a combination of these could have weakened the composites thereby increasing the wearing of the composites by the combined actions of reciprocating movement of the counter body and the particles of PSZ being broken which in-turn grove the attacked surface by increasing the COF (Figure 9).

The results in Figure 8 sufficiently meet expectations; i.e. the higher the reinforcements,

the harder the material until certain percentage composition of the ceramic is reached where third-body mechanism of wear is introduced. Third-body wear mechanisms were activated, and this wear mechanism depends on the wear load and percentage composition of the reinforcements [15]. Ref. [18] also reported that local stresses at the protrusion peak increase with increasing the normal load producing yielding, delamination, and tiny wear debris. Since the sliding amplitude is not large, it is impossible for tiny debris to be completely expelled from the wear surface scar. This trapped debris may both abrade the matrix by ploughing and act as rolling balls. At this point, further addition of the ceramic oxide may not be advised after a certain percentage composition of reinforcement is reached.
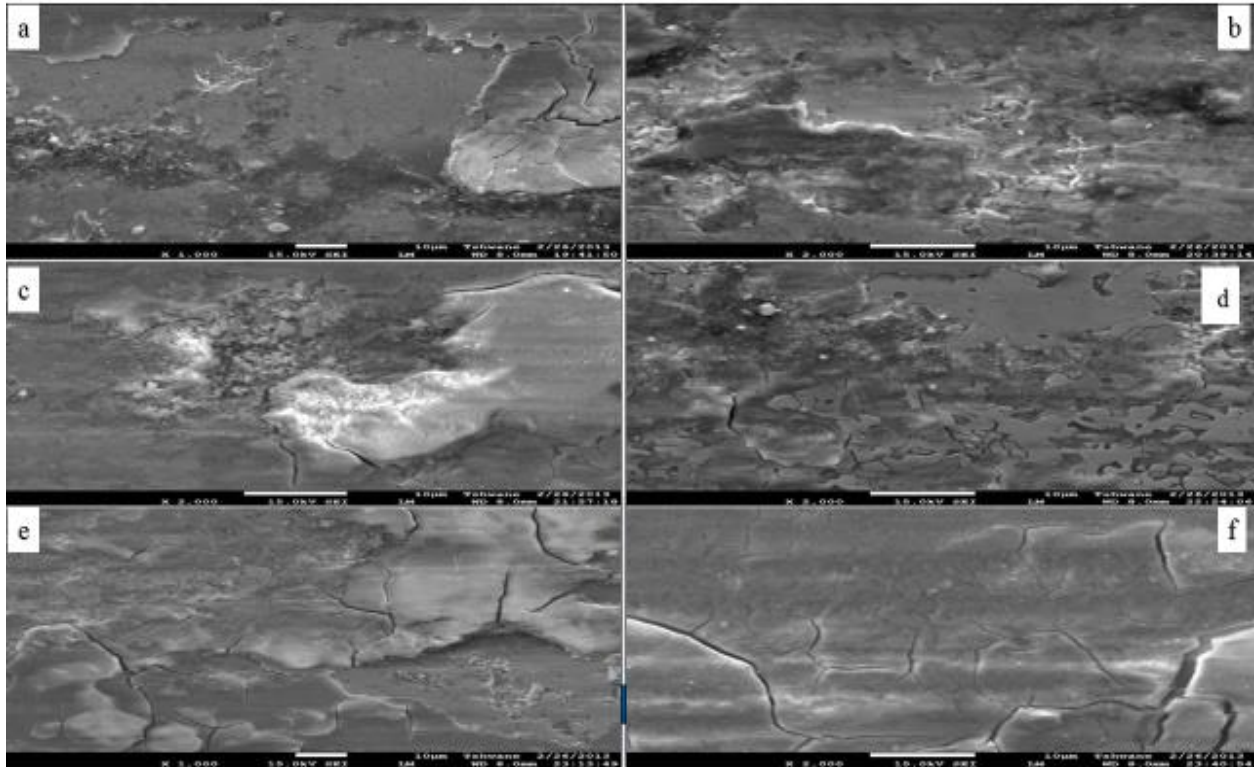

Fig. 9. Scanning electron micrographs of the worn surfaces after wet sliding of (a) A1, (b) A2, (c) A3, (d) A4, (e) A5 and (f) X at 25N.

4-Conclusion

Results revealed that the calculated amount of PSZ addition was found to improve the wear property of the composite. The introduction of the PSZ was found to distort the balance of Cr and Fe which makes the composite to be prone to corrosion. However, further introduction of Cr and Ni helped in arresting this challenge. The results also confirmed the surface imaging capability of SEM and the XRM capability for imaging internal structures, as corroborative tools for understanding corrosion and wear damages. SEM revealed important surface information on the mechanisms of wear damage, while relevant information on pitting corrosion were obtained from XRM technique. SEM and XRM studies showed that pitting corrosion by chloride ions affected both the surfaces and inside of the steel. Detailed pitting information on the internal structures of the ODS DSS steel subjected to chloride attack obtained from XRM revealed that pitting did not result from any oxide inclusion but possibly initiated from chloride attack.

References
1. J. S. Moya, S. Lopez-Esteban, C. Pecharroma´n, "The challenge of ceramic/metal microcomposites and nanocomposites", *Progress in Materials Science,* Vol. 52, 2007, pp. 1017–1090.
2. O. Olaniran, P. Olubambi, J. Potgieter, B, Olaniran, A. Adegbola, D. Folorunso, "Influence of Cr-Ni addition on porosity and microstructure of ZrO2(Y2O3) dispersed duplex stainless steel composite", *Journal of Materials Science and Technology,* Vol. 21, 2013, pp. 186-193.
3. C, Padmavathi, A. Upadhyaya, D. Agrawal, "Corrosion behavior of microwave-sintered austenitic stainless steel composites", *Scripta Materialia*, Vol. 57, 2007, pp. 651–654.
4. M.F. Imbaby, K. Jiang, "Fabrication of free standing 316-L stainless steel–Al2O3 composite micro machine parts by soft moulding" *Acta Materialia*, Vol. 57, 2009, pp. 4751–4757.
5. C. García, F. Martín, P. de Tiedra, C. L. García, "Pitting corrosion behaviour of PM austenitic stainless steels sintered in nitrogen–hydrogen atmosphere", *Corrosion Science,* Vol. 49, 2007, pp. 1718–1736.
6. A. Knote, H.G. Kruger, S. Selve, T.H. Kups, H. Kern, L. Spies, "Metal-ceramic composite layers on stainless steel through the combination of electrophoretic deposition and galvanic process", *Journal of Material Science.* Vol. 42, 2007, pp. 4545-4551.
7. C. Moral, A. Bautista, F. Velasco, " Aqueous corrosion behavior of sintered stainless steels manufactured from mixes of gas atomized and water atomized powder", *Corrosion Science*, Vol. 51, 2009, pp. 1651-1657.
8. P. Datta, G.S. Upadhyaya, "Sintered duplex stainless steels from premixes of 316L and 434L powders", *Materials chemistry and physics,* Vol. 67, 2001, pp. 234-242.
9. C. Molins, J.A. Bas, J. Planas, "PM stainless steel: types and their characteristics and applications", *Advances in Powder Metallurgy*, Vol. 2, 1992, pp. 345-357.
10. Chawla N., Chawla K.K. Metal matrix composites. *Springer*, New York, 2006, p. 15.
11. K.M. Reddy, A. Mukhopadhyaya, B. Basu, "Microstructure-mechanical-tribological property correlation of multistage spark plasma sintered tetragonal ZrO2", *Journal of the European Ceramic Society*, Vol. 30, 2010, pp. 3363-3375.
12. L.A. Dobrzanski, Z. Brytan, A.M. Grande, M. Rosso, "Corrosion resistance of sintered duplex stainless stee evaluated by electrochemical method", Journal *of Achievements in Materials and Manufacturing Engineering,* Vol. 19, 2006, pp. 38-45.
13. W. Chen, J. Zhou, "Preparation and Characterization of Stainless Steel/TiC Nanocomposite Particles by Ball-milling Method", *Journal of Wuhan University of Technology-Mater,* Vol. 43, 2009, pp. *38-41.*
14. C. Garcia, F. Martin, Y. Blanco, M.P. De Tiedra, M.L. Aparicio, "Corrosion behavior of duplex stainless steels sintered in nitrogen"*, Corrosion Science*, Vol. 51, 2009, pp. 76–86.
15. M. Younesi, M.E. Bahroloom, "Optimization of wear resistance and toughness of hydroxyapatite nickel free steel new bio-composites for using in total joint replacement", *Materials and Design,* Vol. 31, 2010, pp. 234-243.
16. J.H. Potgieter, P.A. Olubambi, C.N. Machio, L. Cornish, M.S. El-Sayed, "Influence of nickel additions on the

corrosion behaviour of low nitrogen 22% Cr series duplex stainless steels", *Corrosion Science,* Vol.50, 2008, pp. 2572-2579.

17. S.H. Lau, A. Tkachuk, H. Chang, F, Duewer, H. Cui, M, Feser, W. Yun, Non Invasive, Multi-length Scale Characterization of Smart Materials, Membranes, Sensors with a novel high resolution and high contrast, *ICMAT*, July 2-5, 2007, Singapore.

18. H. Ding, Z, Dai, F. Zhou, G. Zhou, "Sliding friction and wear behaviour of TCII in aqueous condition" *Wear,* Vol. 263, pp. 117-124.